広島大学学術情報リポジトリ
Hiroshima University Institutional Repository

Title	Pseudorotaxanes in the Gas Phase: Structure and Energetics of Protonated Dibenzylamine-Crown Ether Complexes
Author(s)	Kida, Motoki; Shimoyama, Daisuke; Ikeda, Toshiaki; Sekiya, Ryo; Haino, Takeharu; Ebata, Takayuki; Jouvet, Christophe; Inokuchi, Yoshiya
Citation	Physical Chemistry Chemical Physics , 20 (27) : 18678 - 18687
Issue Date	2018-07-11
DOI	10.1039/C8CP02707B
Self DOI	
URL	https://ir.lib.hiroshima-u.ac.jp/00045951
Right	Copyright (c) the Owner Societies 2018 This is the accepted manuscript of the article is available at https://doi.org/10.1039/C8CP02707B This is not the published version. Please cite only the published version. この論文は出版社版でありません。引用の際には出版社版をご確認ご利用ください。
Relation	

Pseudorotaxanes in the Gas Phase: Structure and Energetics of Protonated Dibenzylamine–Crown Ether Complexes

Motoki Kida,[a] Daisuke Shimoyama,[a] Toshiaki Ikeda,[a] Ryo Sekiya,[a] Takeharu Haino,[a] Takayuki Ebata,[a] Christophe Jouvet,[b] and Yoshiya Inokuchi[a,*]

Department of Chemistry, Graduate School of Science, Hiroshima University,

Higashi-Hiroshima, Hiroshima 739-8526, Japan, and CNRS, Aix-Marseille Université,

Physique des Interactions Ioniques et Moléculaires (PIIM), UMR-7345, Marseille,

France

E-mail: y-inokuchi@hiroshima-u.ac.jp

Abstract

We observe UV spectra of protonated dibenzylamine (dBAMH$^+$) and its complexes with 15-crown-5 (dBAMH$^+$–15C5), 18-crown-6 (dBAMH$^+$–18C6), and 24-crown-8 (dBAMH$^+$–24C8) under cold (~10 K) gas-phase conditions by UV photodissociation (UVPD) and UV-UV hole-burning (HB) spectroscopy. The UVPD spectrum of the dBAMH$^+$–15C5 complex shows an extensive low-frequency progression, which originates from a unique conformation of the dBAMH$^+$ part with benzene rings facing closely to each other, while UVPD and calculation results suggest open conformations of the dBAMH$^+$ part for dBAMH$^+$–18C6 and dBAMH$^+$–24C8. UV-UV HB spectra of the dBAMH$^+$–24C8 complex indicate that there exist at least two conformers; multiple conformations can contribute to high stability of dBAMH$^+$–24C8 pseudorotaxane due to "conformational" entropic effects. The UVPD experiment

indicates that the dissociation probability of dBAMH$^+$–24C8 into dBAMH$^+$ and 24C8 is substantially smaller than that of dBAMH$^+$–15C5 and dBAMH$^+$–18C6, which can be related to the barrier height in the dissociation process. The energetics of the dBAMH$^+$–24C8 complex is investigated experimentally with NMR spectroscopy and theoretically with the global reaction route mapping (GRRM) method. An energy barrier of ~60 kJ mol^{-1} is present in the pseudorotaxane formation in solution, whereas there is no barrier in the gas phase. In the course of the photodissociation, excited dBAMH$^+$–24C8 complexes can be trapped at many local minima corresponding to multiple conformations. This can result in effective dissipation of internal energy into degrees of freedom not correlated to the dissociation and decrease the dissociation probability for the dBAMH$^+$–24C8 complex in the gas phase. The energy barrier for the pseudorotaxane formation in solution originates not simply from the slippage process but rather from solvent effects on the dBAMH$^+$–24C8 complex.

*To whom correspondence should be addressed.

[a]Hiroshima University

[b]CNRS, Aix-Marseille Université

1. INTRODUCTION

Rotaxanes are composed of macrocycles threaded by chain-shaped molecules.[1,2] Stoddart and co-workers reported the formation of pseudorotaxanes with dialkylammonium ions and crown ethers in 1995.[3] Since then, a number of studies have been devoted to the synthesis of rotaxanes with dialkylammonium ions and to their applications as molecular machines and polymers.[4-14] Macrocycles with 24 or more atoms, such as dibenzo-24-crown-8 (DB24C8), were frequently used to form rotaxanes with dialkylammonium ions, and the rotaxane formation was confirmed by X-ray diffraction of crystals, mass spectroscopy, and NMR spectroscopy.[3,5,15] The X-ray analysis provided structural information of rotaxanes, but the complex structure in crystals is strongly affected by intermolecular interactions with counteranions and neighboring complexes.[5] Ashton et al. studied thermodynamics and kinetics for the rotaxane formation with secondary dialkylammonium ions and DB24C8 in solution using NMR spectroscopy.[6] They obtained the free energy of association and activation (energy barrier), and the rate constant for the rotaxane formation. The energy barrier corresponds to slippage processes, in which a dialkylammonium ion penetrates the cavity of DB24C8. The stability of rotaxanes is dependent on the nature of the solvent in which it is dissolved.[6] This suggested that solvent effects play certain roles in the rotaxane formation, but a microscopic picture of the solvent effects was not provided in the previous study.[6] As mentioned above, secondary dialkylammonium ions can form rotaxanes with at least 24-membered macrocycles,[5] though Huang and co-workers reported the synthesis of a rotaxane with benzo-21-crown-7 and a dialkylammonium ion.[16] For smaller macrocycles than 24-membered ones, such as 18-crown-6 (18C6), a two-point binding motif was proposed for the complexation with secondary dialkylammonium ions (see Figure 1 of ref. 5); the NH_2^+ center is placed not within the

plane of macrocycles but on it.[5,17-20]   However, this structural motif was not confirmed definitely by X-ray diffraction analysis of crystals.

In this study, we examine the structure and energetics experimentally and theoretically for protonated dibenzylamine (dBAMH$^+$, Scheme 1) and its complexes with 15-crown-5 (dBAMH$^+$–15C5), 18C6 (dBAMH$^+$–18C6), and 24-crown-8 (dBAMH$^+$–24C8) (Scheme 1) under cold (~10 K) gas-phase conditions, which are free from thermal effects, solvent effects, or interactions with counteranions.   dBAMH$^+$ was one of the two dialkylammonium ions that were firstly used to construct pseudorotaxanes with crown ethers in the previous report of Stoddart and co-workers.[3] We perform UV photodissociation (UVPD) spectroscopy of dBAMH$^+$, dBAMH$^+$–15C5, dBAMH$^+$–18C6, and dBAMH$^+$–24C8.   In most of previous studies on pseudorotaxanes with dialkylammonium ions, DB24C8 has been used as a macrocycle.[3,5-7]   In this study, we use 15C5, 18C6, and 24C8, which do not have strong absorption in the UV region.   This enables us to observe purely UV absorption of the dBAMH$^+$ part in the complexes and discuss the effect of the complex formation on the conformation of the dBAMH$^+$ part.   Rijs et al. studied neutral and protonated rotaxanes in the gas phase with a laser desorption or electrospray ion source, collision induced fragmentation, and laser spectroscopy.[21-24]   We produce the ion complexes of dBAMH$^+$ with an electrospray ion source and cool them in a cold quadrupole ion trap in this study.   We previously reported UVPD spectra of dBAMH$^+$, dBAMH$^+$–18C6, and dBAMH$^+$–24C8 at a vibrational temperature of ~30 K.[25]   In the present study, we measure UVPD spectra under colder conditions (~10 K) and narrower laser bandwidths, which will provide sharper band features.   Sharp features of UVPD spectra will allow us to use UV-UV hole-burning (HB) spectroscopy for discriminating vibronic bands of a single isomer.   The number and structure of isomers are determined with the aid of

quantum chemical calculations.[26] In our previous study, we recognized that photodissociation probability of the dBAMH$^+$–24C8 pseudorotaxane was substantially lower than that of the other complexes.[25] We thought that this low probability was related to the potential barrier in the course of rotaxane formation. In this study, we also examine the energetics of the dBAMH$^+$ complexes in solution and in the gas phase to find the origin of the low dissociation probability in the gas phase and the energy barrier in the rotaxane formation.[5,6] We believe that the investigation of the pseudorotaxane in the gas phase would result in highlighting physical/chemical properties of pseudorotaxanes in solution.

2. EXPERIMENTAL AND COMPUTATIONAL METHODS

Details of the experiment for UVPD and UV-UV HB spectroscopy have been described in our previous papers.[27-30] Briefly, the dBAMH$^+$ ion is produced by an electrospray ion source with dBAMH$^+$•SF$_6^-$ salt in methanol (~100 μM). To produce the dBAMH$^+$–15C5, dBAMH$^+$–18C6, or dBAMH$^+$–24C8 complex, one of the crown ethers is added to the methanol solution of dBAMH$^+$•SF$_6^-$ with a concentration of ~100 μM. Dibenzylamine is dissolved in methanol with a protonated form, and ions are directly extracted from the solution with the electrospray ion source. After passing through a vaporization tube and a skimmer, ions are introduced into a cold, Paul-type quadrupole ion trap (QIT). The QIT is cooled to ~4 K by a He cryostat, and He buffer gas is continuously introduced into the QIT. The ions are stored in the QIT for ~50 ms and cooled translationally and internally by the collision with the cold He buffer gas. Ions other than parent ions of interest can be removed from the QIT by an RF potential applied to the entrance end cap.[31] In our experiment of the dBAMH$^+$–crown ether complexes, dominant ions produced by the electrospray ion source are only bare dBAMH$^+$ and the dBAMH$^+$–crown ether complexes. Hence, it is sufficient to remove

bare dBAMH$^+$ from the ion trap in the experiment of the complexes.   The ions are then irradiated by a UV laser, and resulting fragment ions are mass-analyzed and detected with a home-made time-of-flight mass spectrometer.[32]   The UVPD spectra are obtained by plotting yields of the fragment ions against the wavenumber of the UV laser. In this study, we use three types of nanosecond UV laser systems.   Two of the three systems are based on Nd:YAG laser pumped dye lasers (Lambda Physik Scanmate and Continuum ND6000).   Visible outputs from the dye lasers are frequency-doubled, and the UV light is obtained with a resolution of ~0.1 cm^{-1}.   The other UV system is a Nd:YAG laser pumped optical parametric oscillator (EKSPLA NT342B).   The intensity of the output UV light is ~2 mJ/pulse with a repetition rate of 10 Hz and a resolution of ~8 cm^{-1}.   In the UVPD experiments, one of the three UV lasers is used for the photodissociation.   In the UV-UV HB experiment of the dBAMH$^+$ ion, we use the two high-resolution lasers for the pump and the probe light.   The pump laser is introduced to the QIT prior to the probe one by 10–100 μs, and the wavenumber of the pump laser is scanned, while the wavenumber of the probe laser is fixed at one of vibronic bands in the UVPD spectra.   Fragment ions produced with the pump laser are removed by the RF potential applied to the entrance end cap.   The UV-UV HB spectra are obtained by plotting the ratio of the fragment ion intensity with the pump laser on/off (I_{on}/I_{off}) as a function of the wavenumber of the pump laser.[28]   For UV-UV HB spectroscopy of the dBAMH$^+$ complexes, we utilize the low-resolution laser and one of the high-resolution lasers for the pump and probe light, respectively.   We measure ^{1}H NMR spectra of dBAMH$^+$·SF$_6^-$, 15C5, 18C6, 24C8, and their mixtures dissolved in CD$_3$OD or CD$_3$CN at room temperature by using a 300 MHz NMR spectrometer.   The Gibbs free energy for the complex formation of dBAMH$^+$–24C8 in CD$_3$OD and CD$_3$CN is determined on the basis of the ^{1}H NMR spectra.   The barrier height for the complex

formation of dBAMH$^+$–24C8 in CD$_3$OD and CD$_3$CN is obtained by 2D exchange spectroscopy (2D EXSY).[33] The dBAMH$^+$•PF$_6^-$ salt is synthesized by a procedure previously reported by Ashton et al.[5,25] The crown ethers (15C5, 18C6, and 24C8) are purchased from Wako Pure Chemical Industries and used without further purification.

We also perform quantum chemical calculations for dBAMH$^+$, dBAMH$^+$–15C5, dBAMH$^+$–18C6, and dBAMH$^+$–24C8 to examine stable and transition-state structures. Initial conformation searches are performed using the CONFLEX High Performance Conformation Analysis program with the MMFF94s force field.[34-37] Conformers obtained in the initial searches are further optimized with the GAUSSIAN09 program package at the M05-2X/6-31+G(d) level and successively at the M05-2X/6-311++G(d,p) level.[38,39] The vibrational analysis is also carried out at the M05-2X/6-311++G(d,p) level. Electronic transition energies and oscillator strengths of isomers are obtained by time-dependent density functional theory (TD-DFT) calculations at the M05-2X/6-311++G(d,p) level. We used the M05-2X functional because it reproduced the conformer distribution and the position of electronic transitions very well for metal ion–benzo-crown ether complexes in our previous studies.[28,40,41] Furthermore, we obtain the barrier height between stable conformers of dBAMH$^+$ and dBAMH$^+$–24C8 using the global reaction route mapping (GRRM) program with the sphere contracting walk (SCW) and the scaled hypersphere search (SHS) options.[42-45] The GRRM calculations are carried out at the M05-2X/6-31+G(d) level for dBAMH$^+$ and HF/6-31G level for dBAMH$^+$–24C8. Equilibrium and transition-state structures found in the GRRM calculations are further optimized at the M05-2X/6-311++G(d,p) level. The vibrational analysis is also performed at the M05-2X/6-311++G(d,p) level. Calculations in solution are carried out using the polarizable continuum model. For the dBAMH$^+$–15C5 complex, the

Franck-Condon (FC) simulation is performed to reproduce a vibronic structure observed in the UVPD spectrum. We carry out the geometry optimization and vibrational analysis in the S_0 and S_1 states of the dBAMH$^+$–15C5 complex at the ADC(2)/def2-SVP level using the TURBOMOLE program package.[46] The FC simulation is performed with the PGOPHER, a program for simulating rotational, vibrational and electronic spectra.[47]

3. RESULTS AND DISCUSSION

3.1. dBAMH$^+$

Figure 1a shows the UVPD spectrum of the dBAMH$^+$ ion measured using the high-resolution laser with the fragment ion at m/Z = 107 (C$_7$NH$_9^+$) monitored. We previously reported a similar UVPD spectrum of dBAMH$^+$, but the spectrum showed broader band features due to higher ion temperature (~30 K)[48] and lower resolution of the UV laser.[25] The UVPD spectrum in Figure 1a shows three strong bands at 37378, 37464, and 37473 cm^{-1}. Figures 2b and c display the UV-UV HB spectra of dBAMH$^+$ with the UVPD spectrum (Figure 2a). The position of the probe frequencies for the HB spectra is shown with arrows in Figure 2a. The UV-UV HB spectra clearly indicate that two of the three strong bands (37378 and 37473 cm^{-1}) in the UVPD spectrum belong to a single isomer, and that the band at 37464 cm^{-1} is ascribed to another one. Thus, there are at least two isomers for bare dBAMH$^+$.

We determine the structure of bare dBAMH$^+$ with the aid of quantum chemical calculations. Figure 3 shows the optimized structure of dBAMH$^+$. The most stable one (isomer A, Figure 3a) has an open conformation with C$_{2v}$ symmetry. In the second isomer (isomer B, Figure 3b), one of the benzene wings points to the opposite direction to the NH$_2$ group. The third one (isomer C, Figure 3c) has a twisted conformation with C$_2$ symmetry. Since the relative total energy of isomer C (3.0 kJ

mol^{-1}) is higher than that of isomers A and B (0 and 0.6 kJ mol^{-1}, respectively), we can assign the two isomers found in the UVPD experiment to isomers A and B. This assignment is verified by TD-DFT calculations. Figure 2d shows results of TD-DFT calculations for isomers A–C. Each isomer has the S_1–S_0 and S_2–S_0 electronic transitions in this region. In the case of isomer A, only the S_2–S_0 transition emerges strongly, because the S_1–S_0 transition is dipole-forbidden in C_{2V} point group. For isomer B, both of the S_1–S_0 and S_2–S_0 transitions appear with comparable oscillator strengths. Hence, the three strong bands in the UVPD spectrum of dBAMH$^+$ can be reasonably assigned to the electronic transitions of isomers A and B. We did not find isomer B in previous calculations at the M05-2X/6-31+G(d),[25] and we attributed the origin bands in the warmer UVPD spectrum to isomers A and C.[25] However, it is much more reasonable to ascribe the structure of dBAMH$^+$ to isomers A and B on the basis of the total energy calculated with a larger basis set (M05-2X/6-311++G(d,p)) and the agreement of the UVPD spectrum with the TD-DFT results (Figure 2). We check if the structure determination of dBAMH$^+$ described above is reasonable by using another functional including dispersion interaction. Table S2 and Figure S2 in the Electronic Supplementary Information show the relative total energy and TD-DFT results for the dBAMH$^+$ isomers calculated at the ωB97X-D/6-311++G(d,p) level. Isomers A and B of dBAMH$^+$ are the most and the second most stable isomers also at this calculation level (Table S2). The agreement of the transition energy between the calculated and observed spectra seems to be better with the ωB97X-D functional (Figure S2). Hence, the assignment of the structure for bare dBAMH$^+$ to isomers A and B is highly reliable. Figure 4 displays the total energy of stable and transition-state conformations of bare dBAMH$^+$ calculated with the GRRM program. The potential barriers between the three stable isomers are not so high, less than 12 kJ

mol^{-1}.   In the next section, we will show how the complex formation with the crown ethers affects the conformation and electronic transition of dBAMH$^+$.

3.2. dBAMH$^+$–15C5, dBAMH$^+$–18C6, and dBAMH$^+$–24C8

Figures 1b–d display the UVPD spectra of the dBAMH$^+$–15C5, dBAMH$^+$–18C6, and dBAMH$^+$–24C8 complexes.   Spectral features are quite different among the complexes, though the chromophore is dBAMH$^+$ for all the complexes. The UVPD spectrum of the dBAMH$^+$–15C5 complex (Figure 1b) shows an extensive low-frequency progression starting from 37230 cm^{-1} with an interval of ~25 cm^{-1}.   In sharp contrast, the dBAMH$^+$–18C6 complex shows a quite simple spectrum (Figure 1c) with a strong band assignable to the 0-0 transition at 37489 cm^{-1}, suggesting that there is one dominant isomer.   In the case of the dBAMH$^+$–24C8 complex (Figure 1d), there are many sharp bands around 37500 cm^{-1}.   The yields of photofragment dBAMH$^+$ ion are normalized with the intensity of the parent ions and UV laser and are shown in Figures 1b–d as relative values to the maximum of the dBAMH$^+$–15C5 spectrum. Hence, it is possible to compare the vertical axis among the spectra in Figures 1b–d. The photofragment yield of the dBAMH$^+$–24C8 complex is substantially smaller than that of dBAMH$^+$–15C5 and dBAMH$^+$–18C6: only ~10 % of the dBAMH$^+$–15C5 complex.   Similar small quantum yields of the fragmentation were observed for dBAMH$^+$–DB24C6 complex in our previous study.[25]

We determine the number of isomers for the dBAMH$^+$–15C5 and dBAMH$^+$–24C8 complexes by UV-UV HB spectroscopy.   In the HB experiment of the dBAMH$^+$ complexes, we use the low- and high-resolution UV lasers for the pump and probe, respectively, to have deeper depletion in HB spectra.   Before performing UV-UV HB spectroscopy, we check the effect of the laser resolution on the UVPD spectrum of the dBAMH$^+$–15C5 complex.   Figures 5a and b show the UVPD spectra

of the dBAMH$^+$–15C5 complex observed with the high- and low-resolution UV lasers. The vibronic bands in the 37200–37400 cm^{-1} region are resolved even in the low-resolution spectrum (Figure 5b), and the overall features are almost the same between these spectra. Figure 5c displays the UV-UV HB spectrum of the dBAMH$^+$–15C5 complex. The probe position for the UV-UV HB spectrum is shown with an arrow in Figure 5a. As seen in Figures 5b and c, the UVPD and UV-UV HB spectra show the same spectral features. This indicates that the UVPD spectra of the dBAMH$^+$–15C5 complex (Figures 5a and b) can be ascribed to a single isomer. Figure 6 displays the UVPD and UV-UV HB spectra of the dBAMH$^+$–24C8 complex. In the low-resolution UVPD spectrum (Figure 6b), not all the sharp vibronic bands appearing in the high-resolution spectrum (Figure 6a) can be resolved completely, but it is still possible to observe two transitions at 37507 and 37532 cm^{-1} separately. Figures 6c and d depict the UV-UV HB spectra measured at 37507 and 37532 cm^{-1}; the probe positions are shown with arrows in Figure 6a. The signal to noise ratio in the HB spectra of dBAMH$^+$–24C8 is not as high as that of dBAMH$^+$–15C5. However, the HB spectrum measured at 37507 cm^{-1} (Figure 6c) has a dip at 37507 cm^{-1}, accompanied by a few bands around 37680 cm^{-1}. The HB spectrum measured at 37532 cm^{-1} (Figure 6d) shows a clear dip at 37532 cm^{-1} but no depletion at 37507 cm^{-1}. These HB results in Figure 6 indicate that the dBAMH$^+$–24C8 complex has at least two isomers in our gas-phase experiment.

A similar trend of the number of isomers for the dBAMH$^+$ complexes is seen in quantum chemical calculations. Table S1 of the Electronic Supplementary Information shows the relative total energy of stable isomers for the dBAMH$^+$–15C5, dBAMH$^+$–18C6, and dBAMH$^+$–24C8 complexes calculated at the M05-2X/6-311++G(d,p) level. In the case of the dBAMH$^+$–15C5 complex, the energy

difference between the most and the second most stable isomers is substantially large (3.1 kJ mol^{-1}), suggesting that the isomer found in the UVPD experiment can be assigned to the most stable isomer.   In contrast, the dBAMH$^+$–24C8 complex has two stable isomers with almost the same energy, and the energy difference between the second and the third isomers are large (3.5 kJ mol^{-1}).   Hence, the two most stable isomers in the calculations can be attributed to the two isomers found in the experiment. The presence of multiple isomers for the dBAMH$^+$–24C8 complex contributes to high stability of pseudorotaxanes with dBAMH$^+$ and 24C8 because of "conformational" entropic effects; the higher the number of conformers, the more stable the complex.[49] For the dBAMH$^+$–18C6 complex, there exist three isomers with an energy lower than 3 kJ mol^{-1} (Table S1).   As will be described later, the isomer found in the experiment of the dBAMH$^+$–18C6 complex can be ascribed to the most stable form on the basis of the UVPD spectrum.

Results of geometry optimization indicate that the conformation of dBAMH$^+$ is highly affected by the complex formation with 15C5 and 18C6.   Figures 7a and b show the most stable structure of the dBAMH$^+$–15C5 and dBAMH$^+$–18C6 complexes, respectively.   A dominant intermolecular interaction between dBAMH$^+$ and the crown ethers is the NH•••O hydrogen bond for both of the dBAMH$^+$–15C5 and dBAMH$^+$–18C6 complexes, which was proposed in the previous studies.[5,17-20]   On the other hand, one striking difference can be seen in the conformation of the dBAMH$^+$ part, which has not been reported so far.   For the dBAMH$^+$–15C5 complex (Figure 7a), the dBAMH$^+$ part has a conformation similar to isomer C of bare dBAMH$^+$ (Figure 3c); isomer C is the highest energy conformer and is not found in the UVPD experiment of bare dBAMH$^+$.   In the dBAMH$^+$–18C6 complex (Figure 7b), the dBAMH$^+$ part takes a conformation similar to isomer B (Figure 3b).   Intermolecular CH•••π bonds can be

formed in the dBAMH$^+$–18C6 complex; one of the benzene rings in the dBAMH$^+$–18C6 complex has shorter CH•••(benzene centroid) distances (2.49 and 3.49 Å, see Figure 7b).   In the case of the dBAMH$^+$–15C5 complex, the ring size of 15C5 is too small to have an intermolecular CH•••π bond in addition to the NH•••O hydrogen bond.

The extensive low-frequency progression found in the UVPD spectrum of the dBAMH$^+$–15C5 complex (Figure 1b) originates from a unique conformation of the dBAMH$^+$ part in this complex.   We perform the FC simulation for the dBAMH$^+$–15C5 complex to examine the origin of the progression.   Figure 5d displays the FC simulation for the S_1–S_0 transition of the dBAMH$^+$–15C5 complex.   Figures 5e and f depict the equilibrium structure in the S_0 and S_1 states.   As seen in Figure 5d, the progression can be assigned to vibronic transitions at 18 K from vibrational levels of the second lowest-frequency mode (ν_2) in the S_0 state to zero-point vibrational level in the S_1 state.   This assignment can be verified by the difference in the equilibrium structure between the S_0 and S_1 states (Figures 5e and f).   The distance between the two benzene rings becomes substantially shorter from S_0 (~4.7 Å) to S_1 (~3.7 Å).   Since the vector motion of the ν_2 vibration is almost parallel to the structural difference between the S_0 and S_1 states, the ν_2 normal mode becomes active for the S_1–S_0 transition.   There exists a similar normal mode (ν_6) in the S_1 state to the ν_2 vibration in the S_0 state.   In another trial of the FC simulation using the PGOPHER program, the ν_6 mode in the S_1 state is also very active for the S_1–S_0 electronic transition.   However, the simulated progression with the ν_6 mode for the S_1–S_0 transition does not show a parabolic intensity distribution of the progression as seen in the UVPD spectrum (Figure 1b); a vibronic transition to a higher quantum number of the ν_6 mode has a higher intensity in

the S_1–S_0 transition, at least for ν_6 quantum numbers of up to 6. In addition, the frequency of the ν_6 mode in the S_1 state is predicted as 73 cm^{-1}, which is substantially higher than the observed interval of the progression (~25 cm^{-1}). Hence, it is not possible to assign the progression in the UVPD spectrum (Figure 1b) to the ν_6 mode in the S_1 state. The FC simulations for the S_1–S_0 electronic transition cannot reproduce the broad absorption starting from ~37425 cm^{-1}. This broad component can be attributed to the S_2–S_0 transition as shown in Figure 5a.

As mentioned above, the calculation results of the dBAMH$^+$–18C6 complex predict a few low-energy isomers (Table S1). The most stable isomer (Figure 7b) has a form similar to isomer B (Figure 3b) in the dBAMH$^+$ part. In the second and the third most stable isomers, the dBAMH$^+$ part has an isomer C-like form. As can be seen in the UVPD spectrum of the dBAMH$^+$–15C5 complex (Figure 1b), an isomer C form in the dBAMH$^+$ part will show extensive, low-frequency progressions. Since the UVPD spectrum of the dBAMH$^+$–18C6 complex does not show such a progression (Figure 1c), the dBAMH$^+$–18C6 complex in the experiment does not have an isomer C form in the dBAMH$^+$ part. Hence, the structure of the dBAMH$^+$–18C6 complex can be ascribed to the most stable isomer (Figure 7b).

The geometry optimization of the dBAMH$^+$–24C8 complex indicates the predominance of pseudorotaxane forms. Figures 7c and d show the most and the second most stable structures of the dBAMH$^+$–24C8 complex. Different from the dBAMH$^+$–15C5 and dBAMH$^+$–18C6 complexes, the dBAMH$^+$–24C8 complex takes an isomer A-like conformation in the dBAMH$^+$ part. The dBAMH$^+$ component goes through the cavity of the 24C8 part, forming pseudorotaxanes. In the dBAMH$^+$–24C8 complex, several intermolecular CH•••π bonds are formed at both of the benzene rings with a distance shorter than 3.6 Å (see Figures 7c and d). Table 1 shows the binding

energy of the dBAMH[+]–15C5, dBAMH[+]–18C6, and dBAMH[+]–24C8 complexes.   The difference in the binding energy between dBAMH[+]–15C5 and dBAMH[+]–18C6 is 11 kJ mol^{−1}.   The difference between dBAMH[+]–18C6 and dBAMH[+]–24C8 is 48 kJ mol^{−1}, which is more than four times larger than that between dBAMH[+]–15C5 and dBAMH[+]–18C6.   The intermolecular CH•••π bonds between dBAMH[+] and 24C8 play vital roles for high stability (binding energy) of the dBAMH[+]–24C8 complex.

Furthermore, we examine the energetics of the complexes experimentally and theoretically.   It was previously reported that the formation of pseudorotaxanes with dialkylammonium ions and DB24C8 has a barrier of ~80 kJ/mol in solution.[6]   A high barrier may also affect the fragmentation yield after the UV excitation in the UVPD experiment.   Firstly, we obtain the Gibbs free energy experimentally for the formation of dBAMH[+]–24C8 pseudorotaxane in acetonitrile and methanol at room temperature by ^{1}H NMR spectroscopy (Figure 8a).   The energy barrier is estimated as ~60 kJ mol^{−1} in solution.   For the dBAMH[+] complexes in the gas phase, we determine the energetics with quantum chemical calculations.   Figures 8b and c depict the energetics of dBAMH[+]–18C6 and dBAMH[+]–24C8, respectively.   In these figures, dBAMH[+](A) and dBAMH[+](B) stand for isomers A and B of bare dBAMH[+], respectively.   The binding energies of the dBAMH[+]–18C6 and dBAMH[+]–24C8 complexes (198 and 246 kJ mol^{−1}, respectively) are calculated values in this study (Table 1).   The energy of the (18C6 + dBAMH[+](B)) dissociation limit (0.6 kJ mol^{−1}) and the barrier height between (18C6 + dBAMH[+](A)) and (18C6 + dBAMH[+](B)) (8.4 kJ mol^{−1}) are obtained on the basis of the calculated results of bare dBAMH[+] (Figure 4).   The position of the S_1 energy level is derived from the UVPD results in Figure 1.   The barrier height for the formation of dBAMH[+]–18C6 is small (8.4 kJ mol^{−1}); this value corresponds to the isomerization barrier between isomers A and B of bare dBAMH[+].   In the complex formation with

dBAMH$^+$(B) and 18C6, there will be no high barrier; dBAMH$^+$ is simply attached to 18C6 in the complex (Figure 7b). In the case of the dBAMH$^+$–24C8 complex, dBAMH$^+$ has to go through the cavity of 24C8; the barrier for this slipping process is calculated with the GRRM method. In the GRRM calculations, a number of less-stable, pseudorotaxane and non-pseudorotaxane forms are obtained for dBAMH$^+$–24C8, and finally one transition-state structure is found between a pseudorotaxane and a non-pseudorotaxane isomer. Figure 9 shows the structure at the transition state (TS1_2, Figure 9b) and equilibrium structures correlated directly to the transition state (EQ1 and EQ2, Figures 9a and c). Arrows in Figure 9b represent a vector motion of the vibration with an imaginary frequency. This vibration indeed corresponds to the slipping process between the pseudorotaxane (EQ1) and non-pseudorotaxane (EQ2) forms. As seen in Figure 8c, the energy of TS1_2, EQ1, and EQ2 is lower than that of the (dBAMH$^+$ + 24C8) dissociation limit in the gas phase, which is in sharp contrast to the formation in solution (Figure 8a). Upon the UV excitation to the S$_1$ state, the dBAMH$^+$ complexes will dissociate after the internal conversion (IC) to the S$_0$ state followed by the intramolecular vibrational-energy redistribution (IVR). The S$_1$ energy levels of dBAMH$^+$–18C6 and dBAMH$^+$–24C8 are located substantially above the dissociation limit (Figures 8b and c), and the photodissociation of the dBAMH$^+$ complexes will occur with no barrier. As seen in Figure 1, the photofragmentation yield of the dBAMH$^+$–24C8 complex is substantially smaller than that of dBAMH$^+$–15C5 and dBAMH$^+$–18C6. Table 1 shows the transition energy and oscillator strength of the S$_1$–S$_0$ and S$_2$–S$_0$ transitions of dBAMH$^+$, dBAMH$^+$–15C5, dBAMH$^+$–18C6, and dBAMH$^+$–24C8. Since the oscillator strength is comparable for the dBAMH$^+$–15C5, dBAMH$^+$–18C6, and dBAMH$^+$–24C8 complexes, the smaller photofragmentation yield can be ascribed to lower dissociation

16

probability.   In the case of the dBAMH$^+$–24C8 complex, a number of local minima of pseudorotaxane and non-pseudorotaxane forms will exist on the potential energy surface along the photodissociation coordinate.   In the course of the dissociation, hot dBAMH$^+$–24C8 complexes are likely to be trapped at the local minima corresponding to the metastable isomers.   While being trapped at the local minima, hot dBAMH$^+$–24C8 complexes can effectively dissipate their internal energy into degrees of freedom not correlated to the dissociation.   In addition, this trapping process can increase the lifetime of hot dBAMH$^+$–24C8 complexes.   These phenomena will decrease the dissociation probability in a finite time window after the photoexcitation; the ions have to be mass-analyzed within a few μs after the photoexcitation, because the photofragment ions are removed spontaneously from the QIT after the photoexcitation, within ~10 μs, by the RF potential applied to the QIT in our experiment.

The trend of the energetics for the dBAMH$^+$–24C8 pseudorotaxane in solution (Figure 8a) can be reproduced by quantum chemical calculations.   Figure 10 shows calculated energy levels of dBAMH$^+$–24C8 in the gas phase and in methanol.   The Gibbs free energy at 298 K of the transition-state structure (red line in Figure 10) is smaller than that of the dissociation limit, indicating that the formation of dBAMH$^+$–24C8 pseudorotaxane is a barrierless process also in the gas phase at 298 K. In contrast, the Gibbs free energy in methanol at 298 K (green line in Figure 10) shows a noticeable barrier (~67 kJ mol^{-1}) between the pseudorotaxane and the dissociation limit.   As seen in Figures 7c and d, the cationic (NH$_2{}^+$) part of dBAMH$^+$ is fully surrounded by the cavity of 24C8 in dBAMH$^+$–24C8 pseudorotaxanes.   Hence, the stabilization energy due to the solvation in solution will be smaller for dBAMH$^+$–24C8 pseudorotaxanes than that for bare dBAMH$^+$.   In the transition-state form of dBAMH$^+$–24C8 (TS1_2, Figure 9b), since the NH$_2{}^+$ part is slightly displaced from the

24C8 cavity, the stabilization energy of the transition-state form due to the solvation can be between dBAMH$^+$–24C8 pseudorotaxanes and bare dBAMH$^+$. As a result, an energy barrier emerges in the formation of dBAMH$^+$–24C8 pseudorotaxane in solution.

4. SUMMARY

We have measured the UVPD and UV-UV HB spectra of dBAMH$^+$, dBAMH$^+$–15C5, dBAMH$^+$–18C6, and dBAMH$^+$–24C8 under cold conditions in the gas phase. The UVPD spectra of the dBAMH$^+$–15C5, dBAMH$^+$–18C6, and dBAMH$^+$–24C8 complexes show substantially different features from each other. Results of UV-UV HB spectroscopy indicate that the dBAMH$^+$–24C8 complex has at least two conformers, whereas the dBAMH$^+$–15C5 and dBAMH$^+$–18C6 complexes have one dominant isomer each. The existence of multiple stable isomers in the experiment of the dBAMH$^+$–24C8 complex is consistent with the results of quantum chemical calculations showing that there are two low-energy isomers for dBAMH$^+$–24C8, all of which have pseudorotaxane forms. The main intermolecular interaction between dBAMH$^+$ and the crown ethers is the NH•••O hydrogen bond, and effective CH•••π bonds are also involved in high stability of dBAMH$^+$–24C8 pseudorotaxanes. Furthermore, the energetics of the dBAMH$^+$–24C8 complex has been investigated experimentally and theoretically with ^{1}H NMR spectroscopy in solution and the GRRM method. In the pseudorotaxane formation of dBAMH$^+$–24C8, a potential barrier of ~60 kJ mol^{-1} exists in solution, whereas the barrier due to slipping processes is lower in energy than the dissociation threshold in the gas phase. Hence, the energy barrier for the pseudorotaxane formation in solution originates not simply from slippage processes but rather from solvent effects on the dBAMH$^+$–24C8 complex.

**Electronic Supplementary Information:** The calculated total energy of stable isomers for the dBAMH$^+$–15C5, dBAMH$^+$–18C6, and dBAMH$^+$–24C8 complexes. The ^{1}H NMR spectra of dBAMH$^+$, 15C5, 18C6, 24C8, and their mixtures recorded at 300 MHz in CD$_3$OD solution at room temperature. The relative total energy and TD-DFT results of the dBAMH$^+$ isomers calculated at the ωB97X-D/6-311++G(d,p) level.
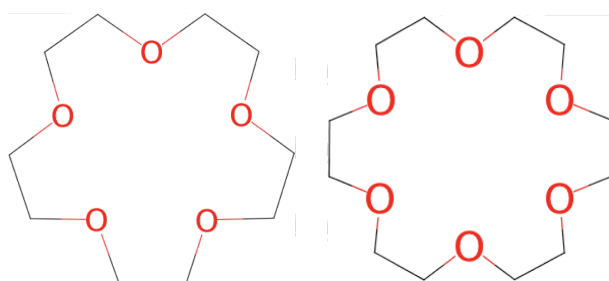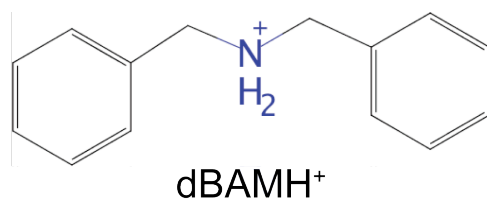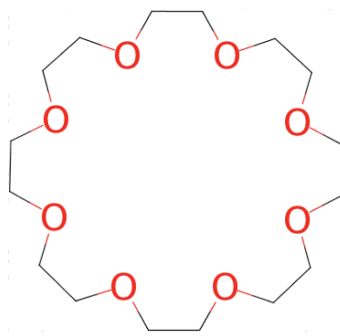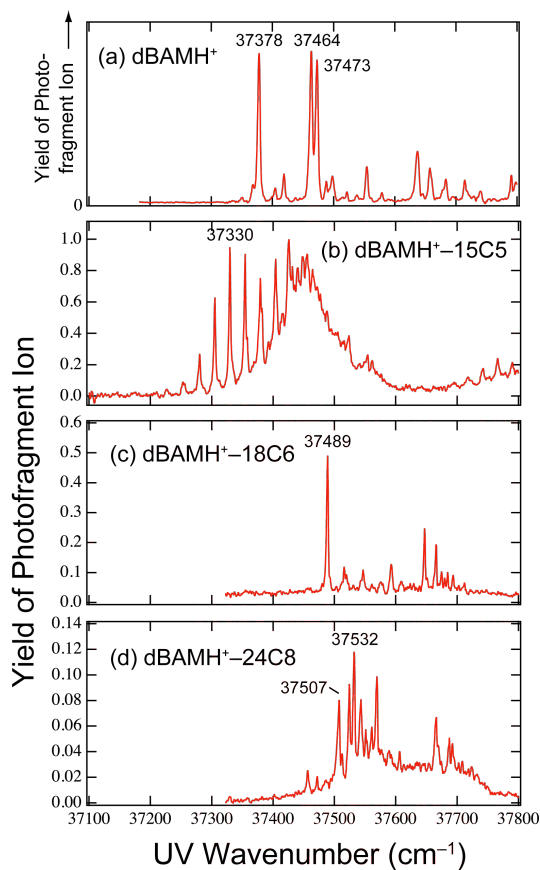
Scheme 1. dBAMH[+], 15C5, 18C6, and 24C8

Figure 1. UVPD spectra of (a) dBAMH$^+$, (b) dBAMH$^+$–15C5, (c) dBAMH$^+$–18C6, and (d) dBAMH$^+$–24C8. We observe the UVPD spectra in Figures 1b–d under the same conditions of the photodissociation (focusing and beam pattern of the UV laser). The UVPD spectrum of dBAMH$^+$ in Figure 1a is measured under different conditions from those of the complexes. Hence, we use different units for the vertical axis between Figures 1a and 1b–d.
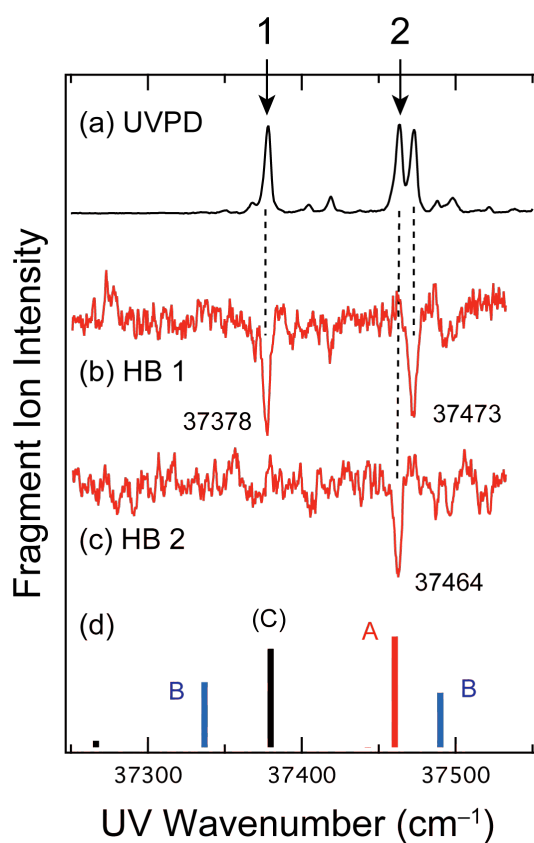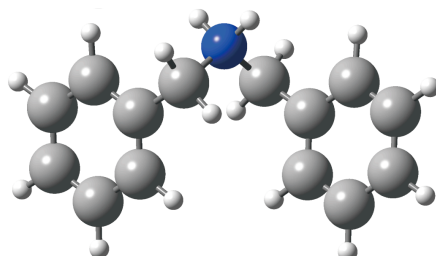
Figure 2. (a) UVPD spectrum of dBAMH^{+}. (b, c) UV-UV HB spectra of dBAMH^{+}. The position of the probe frequencies is shown with arrows in the UVPD spectrum of panel (a). (d) Calculated electronic transitions of dBAMH^{+}. A scaling factor of 0.8331 is used for the calculated transition energy to compare the TD-DFT results with the UVPD spectrum.
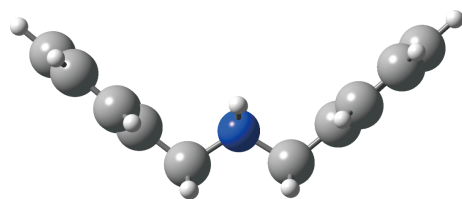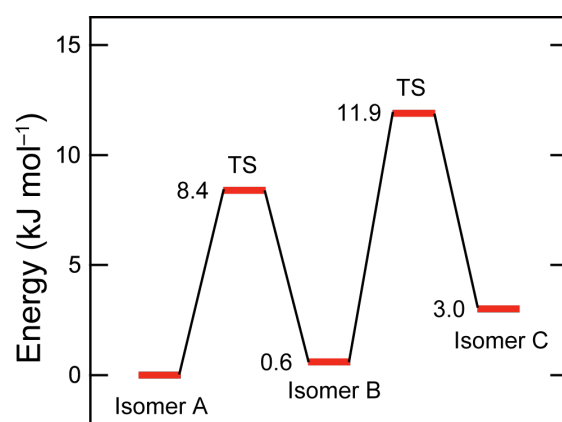
(a) Isomer A (0)
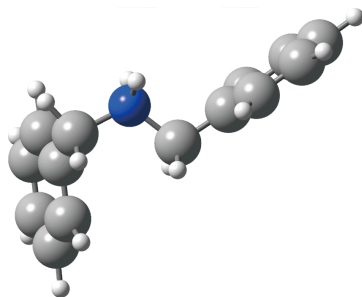
(b) Isomer B (0.6)

(c) Isomer C (3.0)

Figure 3. Structure of bare dBAMH$^+$ calculated at the M05-2X/6-311++G(d,p) level. Numbers in parentheses present the total energy in kJ mol^{-1} relative to that of the most stable isomer (isomer A in panel (a)). The total energy is corrected by zero-point vibrational energy.

Figure 4. Energy levels of stable and transition-state conformations of dBAMH$^+$ calculated at the M05-2X/6-311++G(d,p) level.
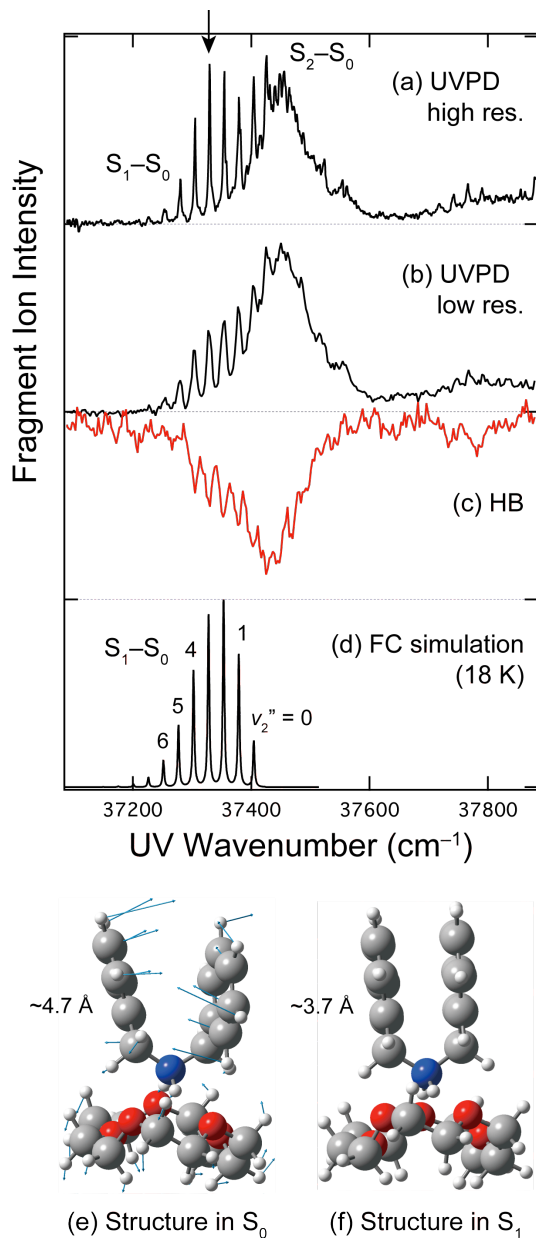
Figure 5. (a) UVPD spectrum of dBAMH$^+$–15C5 with the high-resolution laser. (b) UVPD spectrum of dBAMH$^+$–15C5 with the low-resolution laser. (c) UV-UV HB spectrum of dBAMH$^+$–15C5. The position of the probe frequency is shown with an arrow in the UVPD spectrum of panel (a). (d) FC simulation of the S$_1$–S$_0$ transition of the dBAMH$^+$–15C5 complex. In the FC simulation, the frequency of the ν_2 vibration is scaled by 0.8. (e, f) Calculated equilibrium structure of the dBAMH$^+$–15C5 complex in the S$_0$ and S$_1$ states. Arrows in panel (e) show displacement vectors of the ν_2 vibration in the S$_0$ state. Numbers in the figure show the distance between the centers of the benzene rings.
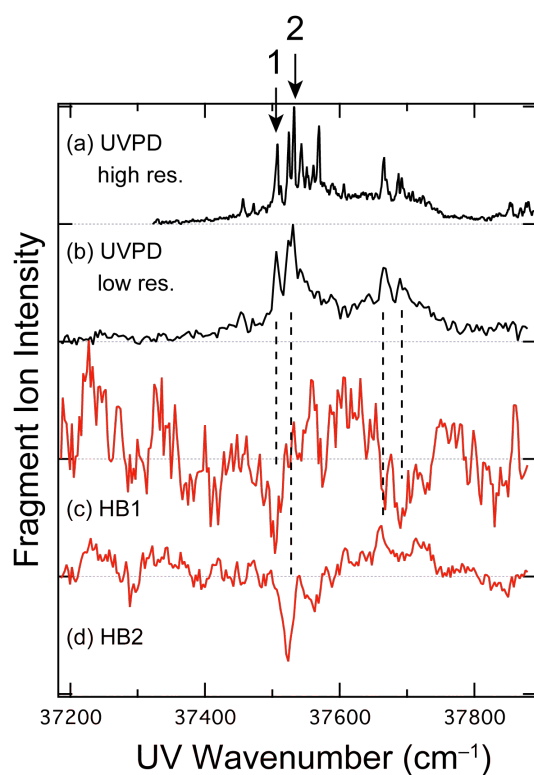
Figure 6. (a) UVPD spectrum of dBAMH$^+$–24C8 with the high-resolution laser.   (b) UVPD spectrum of dBAMH$^+$–24C8 with the low-resolution laser.   (c, d) UV-UV HB spectra of dBAMH$^+$–24C8.   The position of the probe frequencies is shown with arrows in the UVPD spectrum of panel (a).
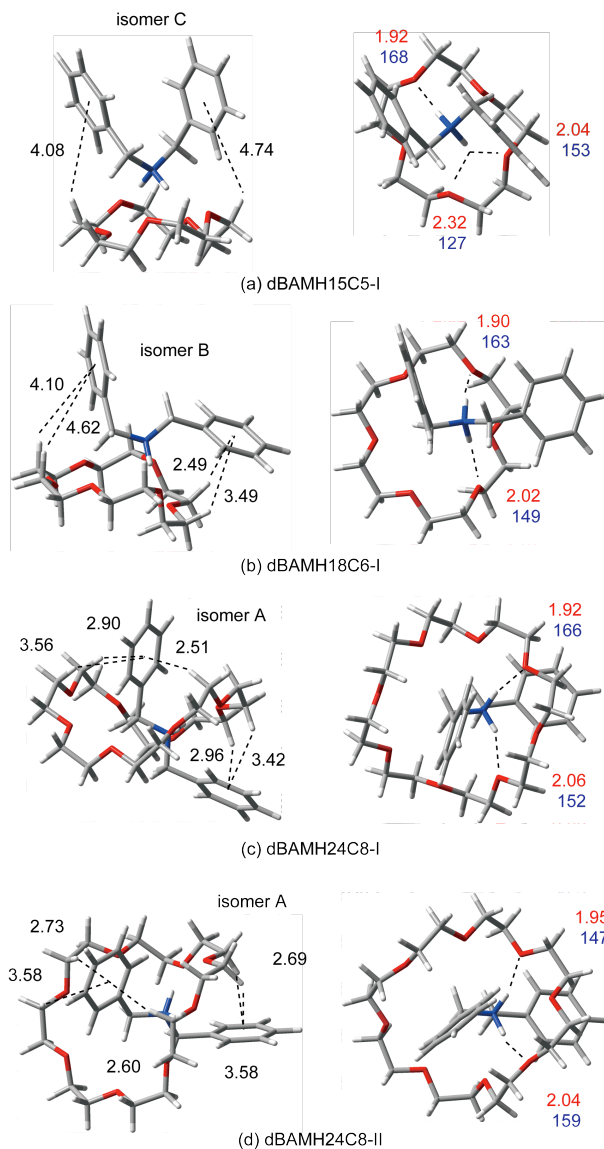
Figure 7. (a, b) Side and top views of the most stable structure for the dBAMH⁺–15C5 and dBAMH⁺–18C6 complexes. (c, d) Side and top views of the most and the second most stable structures for the dBAMH⁺–24C8 complex. Numbers in red, blue, and black represent the NH•••O distance (Å), N–H–O angle (degrees), and CH•••(benzene centroid) distance (Å), respectively. Isomer names shown in the figure (isomers A, B, and C) stand for the conformation of the dBAMH⁺ part in these complexes (see Figure 3).
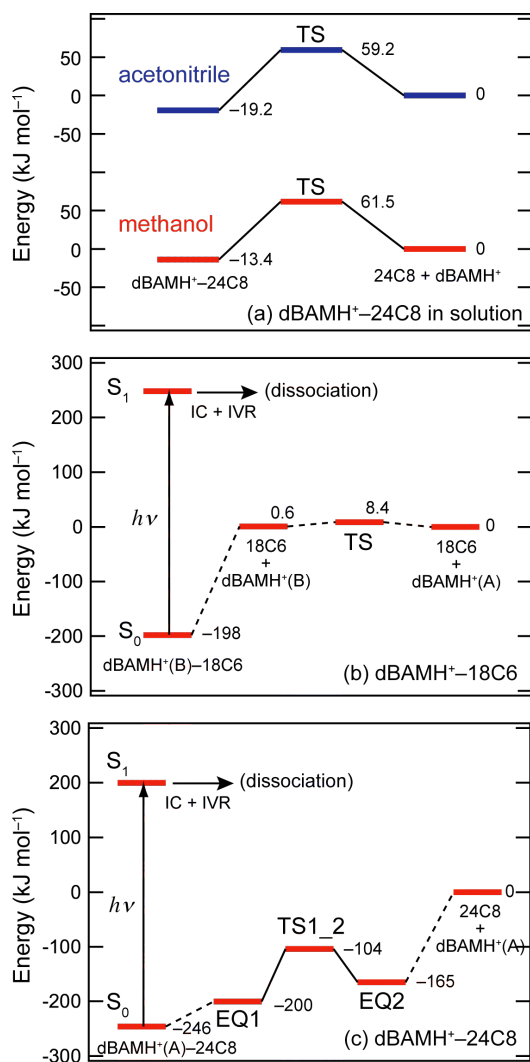
Figure 8. (a) Energetics for the dBAMH$^+$–24C8 complex in methanol and acetonitrile. The energies in panel (a) are obtained experimentally by NMR spectroscopy at room temperature. (b, c) Calculated energetics for the dBAMH$^+$–18C6 and dBAMH$^+$–24C8 complexes in the gas phase at 0 K. The vertical axis represents the energy relative to that of the (18C6 + dBAMH$^+$(A)) or (24C8 + dBAMH$^+$(A)) dissociation limit. The S$_1$–S$_0$ transition energy is determined with the UVPD spectra.
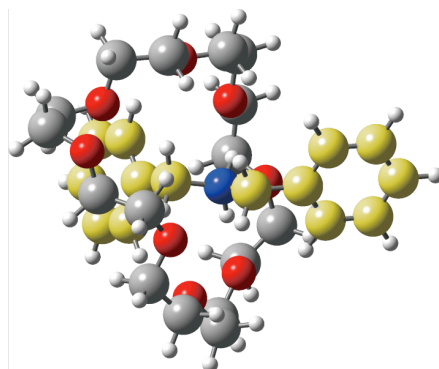
(a) EQ1 (pseudorotaxane)
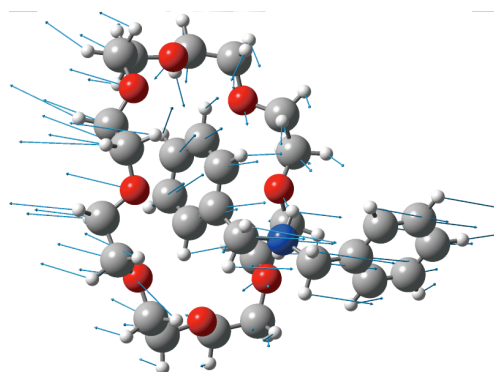
(b) TS1_2
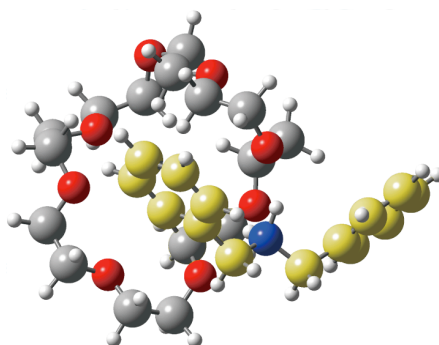
(c) EQ2 (non-pseudorotaxane)

Figure 9. (a, c) Equilibrium structures of the dBAMH$^+$–24C8 complex in the gas phase (EQ1 and EQ2). EQ1 and EQ2 have a pseudorotaxane and non-pseudorotaxane form, respectively. Carbon atoms of the dBAMH$^+$ part are shown in yellow. (b) Transition-state structure of the dBAMH$^+$–24C8 complex between EQ1 and EQ2 (TS1_2). Arrows in panel (b) show displacement vectors of the vibration with an imaginary frequency. EQ1, EQ2, and TS1_2 are found in the GRRM calculations.
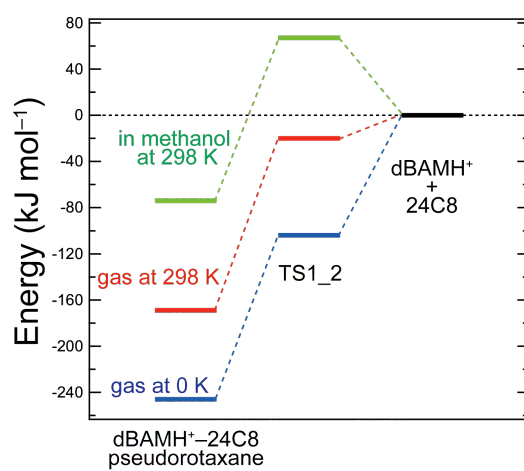
Figure 10. Calculated energy levels related to the dBAMH⁺–24C8 complex in the gas phase and in methanol.   The Gibbs free energy in methanol is obtained using the polarizable continuum model.

Table 1. Binding energy (kJ mol^{-1}), transition energy (eV), and oscillator strength for the S$_1$–S$_0$ and S$_2$–S$_0$ electronic transitions of dBAMH$^+$, dBAMH$^+$–15C5, dBAMH$^+$–18C6, and dBAMH$^+$–24C8 calculated at the M05-2X/6-311++G(d,p) level.

	Binding Energy[a]	S$_1$–S$_0$ transition[b]	S$_2$–S$_0$ transition[b]
dBAMH$^+$ (isomer A)	–	5.57 (0.0000)	5.58 (0.0096)
dBAMH$^+$ (isomer B)	–	5.56 (0.0049)	5.58 (0.0041)
dBAMH$^+$ (isomer C)	–	5.55 (0.0005)	5.56 (0.0074)
dBAMH$^+$–15C5	187	5.50 (0.0052)	5.58 (0.0034)
dBAMH$^+$–18C6	198	5.57 (0.0010)	5.60 (0.0011)
dBAMH$^+$–24C8	246	5.59 (0.0024)	5.59 (0.0015)

[a]The total energy of isomer A (Figure 3a) is used to calculate the binding energy.
[b]Numbers in parentheses are the oscillator strength of the electronic transitions.

TOC entry
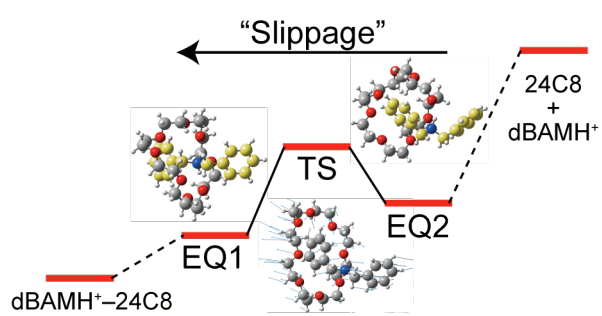
Barrier in the "slippage" process with 24C8 and dBAMH$^+$ is lower than the dissociation threshold in the gas phase.

REFERENCES

1. I. T. Harrison and S. Harrison, *J. Am. Chem. Soc.*, 1967, **89**, 5723-5724.
2. C. J. Bruns and J. F. Stoddart, *The Nature of the Mechanical Bond: From Molecules to Machines*, John Wiley & Sons, Inc., Hoboken, New Jersy, 2016.
3. P. R. Ashton, P. J. Campbell, P. T. Glink, D. Philp, N. Spencer, J. F. Stoddart, E. J. T. Chrystal, S. Menzer, D. J. Williams and P. A. Tasker, *Angew. Chem. Int. Ed.*, 1995, **34**, 1865-1869.
4. P. R. Ashton, P. T. Glink, C. Schiavo, J. F. Stoddart, E. J. T. Chrystal, S. Menzer, D. J. Williams and P. A. Tasker, *Angew. Chem. Int. Ed.*, 1995, **34**, 1869-1871.
5. P. R. Ashton, E. J. T. Chrystal, P. T. Glink, S. Menzer, C. Schiavo, N. Spencer, J. F. Stoddart, P. A. Tasker, A. J. P. White and D. J. Williams, *Chem. Eur. J.*, 1996, **2**, 709-728.
6. P. R. Ashton, I. Baxter, M. C. T. Fyfe, F. M. Raymo, N. Spencer, J. F. Stoddart, A. J. P. White and D. J. Williams, *J. Am. Chem. Soc.*, 1998, **120**, 2297-2307.
7. S. J. Cantrill, D. A. Fulton, A. M. Heiss, A. R. Pease, J. F. Stoddart, A. J. P. White and D. J. Williams, *Chem. Eur. J.*, 2000, **6**, 2274-2287.
8. F. Coutrot and E. Busseron, *Chem. Eur. J.*, 2008, **14**, 4784-4787.
9. F. Coutrot, C. Romuald and E. Busseron, *Org. Lett.*, 2008, **10**, 3741-3744.
10. C.-C. Hsu, N.-C. Chen, C.-C. Lai, Y.-H. Liu, S.-M. Peng and S.-H. Chiu, *Angew. Chem. Int. Ed.*, 2008, **47**, 7475-7478.
11. F. Coutrot and E. Busseron, *Chem. Eur. J.*, 2009, **15**, 5186-5190.
12. C. Romuald, A. Arda, C. Clavel, J. Jimenez-Barbero and F. Coutrot, *Chem. Sci.*, 2012, **3**, 1851-1857.
13. M. Xue, Y. Yang, X. Chi, X. Yan and F. Huang, *Chem. Rev.*, 2015, **115**, 7398-7501.
14. Z. Zhou, X. Yan, T. R. Cook, M. L. Saha and P. J. Stang, *J. Am. Chem. Soc.*, 2016, **138**, 806-809.
15. S. Ganguly and H. W. Gibson, *Macromolecules*, 1993, **26**, 2408-2412.
16. C. Zhang, S. Li, J. Zhang, K. Zhu, N. Li and F. Huang, *Org. Lett.*, 2007, **9**, 5553-5556.
17. R. M. Izatt, J. D. Lamb, N. E. Izatt, B. E. Rossiter, J. J. Christensen and B. L. Haymore, *J. Am. Chem. Soc.*, 1979, **101**, 6273-6276.
18. J. C. Metcalfe, J. F. Stoddart and G. Jones, *J. Am. Chem. Soc.*, 1977, **99**, 8317-8319.
19. J. Krane and O. Aune, *Acta Chem. Scand.*, 1980, **B34**, 397-401.
20. H. Tsukube, *Bull. Chem. Soc. Jpn.*, 1984, **57**, 2685-2686.
21. A. M. Rijs, B. O. Crews, M. S. de Vries, J. S. Hannam, D. A. Leigh, M. Fanti, F. Zerbetto and W. J. Buma, *Angew. Chem. Int. Ed.*, 2008, **47**, 3174-3179.
22. A. M. Rijs, N. Sändig, M. N. Blom, J. Oomens, J. S. Hannam, D. A. Leigh, F. Zerbetto and W. J. Buma, *Angew. Chem. Int. Ed.*, 2010, **49**, 3896-3900.
23. A. M. Rijs, I. Compagnon, A. Silva, J. S. Hannam, D. A. Leigh, E. R. Kay and P. Dugourd, *Phys. Chem. Chem. Phys.*, 2010, **12**, 12556-12561.
24. A. M. Rijs, E. R. Kay, D. A. Leigh and W. J. Buma, *J. Phys. Chem. A*, 2011, **115**, 9669-9675.
25. Y. Inokuchi, T. Haino, R. Sekiya, F. Morishima, C. Dedonder, G. Feraud, C. Jouvet and T. Ebata, *Phys. Chem. Chem. Phys.*, 2015, **17**, 25925-25934.
26. K. Ohashi, Y. Inokuchi and N. Nishi, *Chem. Phys. Lett.*, 1996, **263**, 167-172.

27. Y. Inokuchi, K. Soga, K. Hirai, M. Kida, F. Morishima and T. Ebata, *J. Phys. Chem. A*, 2015, **119**, 8512-8518.
28. Y. Inokuchi, M. Nakatsuma, M. Kida and T. Ebata, *J. Phys. Chem. A*, 2016, **120**, 6394-6401.
29. Y. Inokuchi, M. Kida and T. Ebata, *J. Phys. Chem. A*, 2017, **121**, 954-962.
30. Y. Inokuchi, K. Hirai and T. Ebata, *Phys. Chem. Chem. Phys.*, 2017, **19**, 12857-12867.
31. H. Kang, G. Féraud, C. Dedonder-Lardeux and C. Jouvet, *J. Phys. Chem. Lett.*, 2014, **5**, 2760-2764.
32. Y. Kobayashi, Y. Inokuchi and T. Ebata, *J. Chem. Phys.*, 2008, **128**, 164319.
33. C. L. Perrin and T. J. Dwyer, *Chem. Rev.*, 1990, **90**, 935-967.
34. H. Goto and E. Osawa, *J. Am. Chem. Soc.*, 1989, **111**, 8950-8951.
35. H. Goto and E. Osawa, *J. Chem. Soc. Perkin Trans. 2*, 1993, 187-198.
36. Y. Inokuchi, T. Ebata and T. R. Rizzo, *J. Phys. Chem. A*, 2015, **119**, 8097-8105.
37. Y. Inokuchi, T. Ebata, T. Ikeda, T. Haino, T. Kimura, H. Guo and Y. Furutani, *New J. Chem.*, 2015, **39**, 8673-8680.
38. M. J. Frisch, G. W. Trucks, H. B. Schlegel, G. E. Scuseria, M. A. Robb, J. R. Cheeseman, G. Scalmani, V. Barone, B. Mennucci, G. A. Petersson, H. Nakatsuji, M. Caricato, X. Li, H. P. Hratchian, A. F. Izmaylov, J. Bloino, G. Zheng, J. L. Sonnenberg, M. Hada, M. Ehara, K. Toyota, R. Fukuda, J. Hasegawa, M. Ishida, T. Nakajima, Y. Honda, O. Kitao, H. Nakai, T. Vreven, J. Montgomery, J. A., J. E. Peralta, F. Ogliaro, M. Bearpark, J. J. Heyd, E. Brothers, K. N. Kudin, V. N. Staroverov, R. Kobayashi, J. Normand, K. Raghavachari, A. Rendell, J. C. Burant, S. S. Iyengar, J. Tomasi, M. Cossi, N. Rega, N. J. Millam, M. Klene, J. E. Knox, J. B. Cross, V. Bakken, C. Adamo, J. Jaramillo, R. Gomperts, R. E. Stratmann, O. Yazyev, A. J. Austin, R. Cammi, C. Pomelli, J. W. Ochterski, R. L. Martin, K. Morokuma, V. G. Zakrzewski, G. A. Voth, P. Salvador, J. J. Dannenberg, S. Dapprich, A. D. Daniels, Ö. Farkas, J. B. Foresman, J. V. Ortiz, J. Cioslowski and D. J. Fox, *Gaussian 09, Revision A.02,* 2009.
39. Y. Zhao, N. E. Schultz and D. G. Truhlar, *J. Chem. Theory Comput.*, 2006, **2**, 364-382.
40. Y. Inokuchi, O. V. Boyarkin, R. Kusaka, T. Haino, T. Ebata and T. R. Rizzo, *J. Am. Chem. Soc.*, 2011, **133**, 12256-12263.
41. Y. Inokuchi, O. V. Boyarkin, R. Kusaka, T. Haino, T. Ebata and T. R. Rizzo, *J. Phys. Chem. A*, 2012, **116**, 4057-4068.
42. K. Ohno and S. Maeda, *Chem. Phys. Lett.*, 2004, **384**, 277-282.
43. S. Maeda and K. Ohno, *J. Phys. Chem. A*, 2005, **109**, 5742-5753.
44. K. Ohno and S. Maeda, *J. Phys. Chem. A*, 2006, **110**, 8933-8941.
45. S. Maeda and K. Ohno, *J. Chem. Phys.*, 2006, **124**, 174306.
46. R. Ahlrichs, M. Bär, M. Häser, H. Horn and C. Kölmel, *Chem. Phys. Lett.*, 1989, **162**, 165-169.
47. C. M. Western, *J. Quant. Spectrosc. Radiat. Transfer*, 2017, **186**, 221-242.
48. C. Dedonder, G. Féraud and C. Jouvet, *J. Chem. Phys.*, 2014, **141**, 131101.
49. Y. Inokuchi, T. Ebata, T. R. Rizzo and O. V. Boyarkin, *J. Am. Chem. Soc.*, 2014, **136**, 1815-1824.